

# Growth kinetics in two-dimensional binary mixtures with bond-disorder: Monte Carlo simulation results

Samiksha Shrivastava and Awaneesh Singh\*

Department of Physics, Indian Institute of Technology (BHU), Varanasi-221005, India

## Abstract

The evolving domain structures in phase separating mixtures can significantly influence the final properties of materials. We present here the effect of quenched disorder (in the form of bond-disorder) on the kinetics of phase separating binary (*AB*) mixtures. Our particular focus is on the domain structure, phase behavior, growth laws, and dynamical scaling. The bond disorder (BD), which acts as an impurity in the system, is introduced in a regular manner. To model the evolution kinetics, we utilize the well-known conserved spin-exchange (Kawasaki) kinetics on a two-dimensional (*2d*) Ising system via an extensive Monte Carlo (MC) simulation study. The effect of BD is analyzed for the critical (*AB*) mixtures. We observed that the dynamical scaling, exhibited by the scaled correlation function and the corresponding structure factor, changes by varying the number of disordered sites at different temperatures below the critical temperature ( $T_c$ ). When the system is deeply quenched at the lower BD sites, we hardly observed any significant effect on the phase separation kinetics and domain morphologies. However, in the presence of a higher BD, the evolution morphologies illustrate lamellar (anisotropic) patterns at all the temperatures studied here below  $T_c$ .

**Keywords:** Ising model, Kawasaki kinetics, critical mixture, phase separation, bond-disorder.

\*Author for correspondence: [awaneesh.phy@iitbhu.ac.in](mailto:awaneesh.phy@iitbhu.ac.in); [awaneesh11@gmail.com](mailto:awaneesh11@gmail.com)

## 1. Introduction

A binary (*AB*) mixture stays in a homogeneous (disordered) state at high temperatures ( $T \gg T_c$ ) due to high entropic contribution from the thermodynamic relation  $F = E - TS$ . Here,  $F$  and  $E$  denote Helmholtz free energy and the internal energy of the system, respectively. The temperature and the entropy of the system are marked by  $T$  and  $S$  respectively.  $T_c$  implies the critical temperature at which the Ising system changes its physical behavior (e.g., order-disorder transition in the binary alloy, phase separation in the binary mixture, etc.). [1–3] When a homogeneous mixture is quenched below the critical temperature ( $T \ll T_c$ ), it becomes thermodynamically unstable due to small inhomogeneities initiated within the system; the phase separation in this far-from-equilibrium system begins either by the spinodal decomposition (SD) [1–5] or by the nucleation and growth (NG) [2–5] enriched in either component.

The kinetics of phase separation has been a well-studied subject of interest for decades, focusing on the coarsening of binary mixtures utilizing experimental [6–8], analytical [2,9], and simulation methods. [10–14] Nonetheless, this remains an active and robust area of research. [15–20] To specify the coarsening morphologies, one typically calculates the following two crucial physical quantities of practical importance; (i) the two-point equal-time correlation function  $C(\vec{r}, t)$  where  $\vec{r} = \vec{r}_1 - \vec{r}_2$  and its Fourier transforms, the structure factor  $S(\vec{k}, t)$  where  $\vec{k}$  represents the wave vector [1,2]; (ii) the domain growth law: time evolution of characteristic domain size, which depends on a few common system properties such as conservation laws, hydrodynamic velocity field [21,22], and the presence of quenched or annealed disorder. [16,23–27]

The domain growth law of a pure isotropic system is widely investigated and explained, which typically follows power-law behavior:  $\ell(t) \sim t^\phi$  at late times when larger domains grow at the cost of the smaller ones; here  $\phi$  denotes the growth exponent [1,2]. The value of  $\phi$  depends on the mechanism that drives the domain coarsening. For the diffusion-driven phase separation kinetics of *AB* mixture where the concentration of *A* and *B* phases are conserved, the rate of domain evolution scales as  $\dot{\ell}(t) \sim |\vec{\nabla}\mu| \sim \sigma/\ell(t)^2$  provides  $\ell(t) \sim t^{1/3}$ ; this is commonly known as the Lifshitz-Slyozov (LS) growth law with growth exponent:  $\phi = 1/3$ . [1–3,28] Here,  $\dot{\ell}(t)$  is the interface velocity,  $\mu$  is the chemical potential, and  $\sigma$  is the interfacial tension between the phases. Nonetheless, with hydrodynamic effects comprised in the system, various growth regimes appear depending on the dimensionality and the other system parameters [21,22,29–31].

Typically, it is hard to find a pure and isotropic experimental system as it always comprises some impurities (annealed or quenched). In this context, a few essential analytical and numerical studies are performed on the *2d* Ising model with the quenched disorder [9–12,23–25]. The quench-disorder is considered as an immobile impurity in the system; it is introduced in a pure Ising system in the following way: (i) the random-bond Ising model (RBIM) [12,23–25] using *nn* spin-exchange kinetics, and (ii) the random-field Ising model (RFIM) [32–35]. In general, the disordered sites trap domain boundaries and result in slower domain growth. A critical study of RBIM for the non-conserved system is done by Huse and Henley (HH) [27]. They argued that the energy barrier that traps evolving domain boundaries follows power-law dependence on domain size. The characteristic length scale turns out to follow a logarithmic behavior:  $R(t) \sim (\ln t)^\phi$ . Subsequently, many experimental [6–8] and simulation [9–14,25,26] works were performed to assess HH proposal without explicitly confirming the universal

logarithmic growth law in the asymptotic regime. Nevertheless, a power-law growth with the variable exponent is suggested instead.

Later, Paul, Puri, and Rieger (PPR) revisited the RBIM problem in detail using Monte Carlo (MC) simulations with non-conserved spin-flip kinetics and conserved spin-exchange kinetics [23,24]. PPR proposed that the energy barrier for trapping domain boundaries follows logarithmic dependence on the domain size instead of a power law [23,24]. In contrast to HH observation, PPR showed a power-law dependence on the average domain size where growth exponent depends on the quench depth and impurities in the system; these results were further confirmed experimentally [6–8]. Overall, due to the small average domain size at early times, the energy barrier becomes negligible, and hence, the system evolves like a pure system. However, after a crossover length scale at late times, disorder traps become effective due to a higher energy barrier [27]. Therefore, domain coarsening occurs via thermal activation over the corresponding energy barrier. Thus, thermal fluctuations drive the domain growth at late times [23,24]; this contrasts with the pure case, where thermal fluctuations are irrelevant.

Nonetheless, HH and PPR have introduced the quenched disorder by uniformly varying,  $J_{ij}$ , between zero and one for all the lattice sites [23,24,27]. Moreover, we recently studied the quenched disorder for the  $2d$  Ising system, where BD was introduced in two different manners: a) randomly, and b) regularly selected lattice sites [16];  $J_{ij}$  was set to zero for the disordered sites and one for the rest. We explored the effect of disorder on the growth kinetics and domain structure by performing MC simulations only for a given shallow quench depth using non-conserved (spin-flip) and conserved (spin-exchange) kinetics. The average domain size illustrated a normal power-law (LS) growth where the growth exponent depends on the number of disordered sites in the system. However, the influence of quench disorder mainly for the lower percentages and at various quench depths was unexplored in the asymptotic time limit.

This paper systematically presents a comparative study of domain coarsening for the conserved  $2d$  Ising system (binary mixture) with BD introduced at regularly selected lattice sites via extensive MC simulations. In particular, we studied the effect of various deep and shallow quench depths and the number of disordered sites on the evolution kinetics and dynamical scaling. Our focus is to understand the domain growth and universality in the system with bond-disorder where theoretical calculations, in general, are complex at present.

We organize this paper as follows. First, in Sec. 2, we explain the numerical methodology used to simulate the system. Then, Sec. 3 presents the results and discussions for different

temperatures and the number of BD. Finally, in Sec. 4, we conclude this paper with a summary of our results.

## 2. Simulation model and implementation

**Basic setup with disordered sites:** MC simulation method is utilized to study the effect of BD in the  $2d$  Ising system. The Hamiltonian is given by

$$H = - \sum_{\langle ij \rangle} J_{ij} S_i S_j - \sum_{i=1}^N h_i S_i, \quad S_i = \pm 1 \quad (1)$$

where  $S_i$  denotes the spin at  $i^{th}$  lattice site. It can take values,  $S_i = +1$  (up spin state) when the  $i^{th}$  site is occupied by  $A$ -type atom, and  $S_i = -1$  (down spin state) when it is occupied by  $B$ -type atom. The parameter,  $J_{ij}$  represents the spin-exchange interaction strength, and  $\langle ij \rangle$  indicates the sum over  $nn$  spins. In general,  $J_{ij} > 0$  is set for a ferromagnetic system and  $J_{ij} < 0$  for an antiferromagnetic system; however, a system with both ferromagnetic and antiferromagnetic exchange coupling, usually relevant to spin glasses. The external field in the simulation is set to zero ( $h_i = 0$ ); nevertheless,  $h_i \neq 0$  for  $J_{ij} > 0$  case is known as RFIM [32–35], one of the most straightforward Ising systems with quenched disorder. In our MC simulation, we set,  $J_{ij} = 1$  for a pure system. The scaled critical temperature for the  $2d$  Ising system is set to  $k_B T_c / J_{ij} \approx 2 / \ln(1 + \sqrt{2})$  ( $= 2.269$ ) obtained from the Onsager's exact solution of the Ising model on a square lattice with  $nn$  interactions; [36]  $k_B$  denotes the Boltzmann constant. For a disordered system,  $J_{ij} = 0$ , which corresponds to the system at  $T \gg T_c$ .

We choose a square lattice of size,  $N = L_x \times L_y$  with periodic boundary conditions in both the directions where  $L_x = L_y = 512$ . The indexes  $i = 1 \dots L_x$  and  $j = 1 \dots L_y$  denotes the lattice point positions in the  $x$  and  $y$ -directions, respectively. The disorder in the system is introduced by the exchange coupling parameter,  $J_{ij} = 1 - \varepsilon_{ij}$  where  $\varepsilon_{ij}$  represents the degree of disorder. [16] For simplicity, we considered  $\varepsilon_{ij} = 0$  for the pure site and  $\varepsilon_{ij} = 1$  for the disordered site, which corresponds to the system's impurity. [16,37] Hence,  $J_{ij} = 1$  for the pure sites, and  $J_{ij} = 0$  for the disordered sites. Note that in PPR's quench disorder [23,24] study, a uniform distribution of  $J_{ij} \in [0,1]$  was considered. To introduce the disorder, we select a fraction of sites in a regular manner. For every lattice index,  $i$  from  $1 \dots L_x$ , we traced the index,  $j$  from  $1 \dots L_y$  and in the process every  $m^{th}$  site is tagged as the disorder site with a degree of disorder,  $\varepsilon_{ij} = 1$ . The remaining sites are considered as the pure sites,  $\varepsilon_{ij} = 0$ . Thus, the total number of disordered sites in a system is,  $N_1 = N/m$  [16].

The initial configuration of the critical  $AB$  mixture has a random distribution of  $A$  ( $S_i = +1$ ) and  $B$  ( $S_i = -1$ ) atoms on the lattice sites such that the density,  $\rho = 1.0$ ; this corresponds to a homogeneous state of the system at a high temperature ( $T \gg T_c$ ). The Ising system itself does not have an intrinsic dynamic; hence, we place it in contact with a heat bath to associate with the stochastic dynamics. [1–3] Thus, the resultant model is referred to as a *kinetic Ising model*. [1] The homogeneous system is then quenched below  $T_c$  for the evolution to take place. We probe the effect of disorder on the growth kinetics with various quench depths:  $T = 0.5$ , 1.0, and 1.5, respectively. Here,  $T = 0.5$  is referred to as deep quench, and  $T = 1.5$  is shallow quench. Shortly, we present the results for three percentages of disorder,  $N_1 = 2\%$ , 5%, and 10% of  $N$  and compare them with the pure case,  $N_1 = 0\%N$ .

We exploit the Kawasaki (spin-exchange) kinetics to model the phase separation in binary ( $AB$ ) mixture. For a single MC move, we randomly select two  $nn$  sites with opposite spins to exchange them ( $S_i \leftrightarrow S_j$ ). The energy change for a spin-exchange to take place is computed as [38]

$$\Delta H_{ij} = 2 S_i \left[ \sum_{i' \neq j}^q J_{ii'} S_{i'} - \sum_{j' \neq i}^q J_{jj'} S_{j'} \right]. \quad (2)$$

Here  $q$  denotes the coordination number of a site. The move is then accepted or rejected with the standard Metropolis acceptance probability [38,39]:

$$P = \begin{cases} e^{-\beta \Delta H_{ij}}, & \Delta H_{ij} > 0 \\ 1, & \Delta H_{ij} \leq 0 \end{cases}; \quad (3)$$

where,  $\beta = 1/k_B T$ . A single Monte Carlo step (MCS) is completed when the Metropolis algorithm is executed  $N$  number of times, independent of whether the spin-exchange move is accepted or rejected. Note that we accept the proposed spin-exchange with  $P = 1$  if any spin from a randomly selected pair belongs to the disordered sites.

**Correlation function and structure factor:** To characterize the evolution morphology and the length scale, we compute the two-point equal-time correlation function [1,2], which measures the overlap of spin configuration at a distance  $\vec{r}$ :

$$C(\vec{r}, t) = \frac{1}{N} \sum_i [\langle S_i(t) S_{i+\vec{r}}(t) \rangle - \langle S_i(t) \rangle \langle S_{i+\vec{r}}(t) \rangle]. \quad (4)$$

The angular brackets represent the statistical averaging of data. The structure factor, an experimentally more relevant physical parameter to study the domain morphology, is the Fourier transform of  $C(\vec{r}, t)$  [1,2]:

$$S(\vec{k}, t) = \sum_{\vec{r}} e^{i\vec{k} \cdot \vec{r}} C(\vec{r}, t), \quad (5)$$

where  $\vec{k}$  represents the scattering wave vector. When the evolved morphologies are isotropic, the correlation function and the structure factor statistics can be improved by spherical averaging. The corresponding quantities are denoted as  $C(r, t)$ , and  $S(k, t)$ , respectively, where  $r$  is the separation between two spatial points and  $k$  is the magnitude of the wave-vector. The correlation function and the structure factor data are spherically average over ten independent runs unless stated otherwise. For the anisotropic morphologies in the system, we compute the component of the structure factor in different directions.

**Scaling functions and length scale:** The domain coarsening is a well-established scaling phenomenon characterized by a unique length scale,  $\ell(t)$ . The dynamical scaling form of the correlation function and the structure factor are as follows:

$$C(r, t) \sim g[r/\ell(t)], \quad (6)$$

$$S(k, t) \sim \ell(t)^d f[k\ell(t)], \quad (7)$$

where  $g(x)$  and  $f(p)$  are scaling functions. The characteristic length scale,  $\ell(t)$ , is estimated from the correlation function as the distance over which it decays to zero or a fraction of its maximum value,  $C(0, t) = 1$ . [15] We find that the decay of  $C(r, t)$  to 0.1 gives a good measure of  $\ell(t)$ . A few other definitions of length scale are (i) inverse of the first moment of the structure factor [15], (ii) the first moment of normalized domain-size distribution. [40,41] Nevertheless, they differ only by constant multiplicative factors in the scaling regime [15,40,41]. We extracted the asymptotic growth exponent by computing an effective growth exponent as follows [27,42,43]:

$$\phi_{eff} = \log_{\alpha} \left[ \frac{\ell(at)}{\ell(t)} \right], \quad (8)$$

where we set the log-base  $\alpha = 2$ .

### 3. Simulation results and discussion

We quench the system at  $t = 0$  MCS from a high-temperature homogeneous phase to a temperature,  $T < T_c$ , and monitored the coarsening at various MCS. In displaying these results, we focus on (i) probing the effects of different  $N_1$  (0%, 2%, 5%, 10%) on coarsening morphologies at various quench depths ( $T < T_c$ ), and (ii) how  $N_1$  and quench depths influence the characteristic growth laws and scaling behavior of the system.

#### i. Pure mixture: $\epsilon = 0$

At the outset of our simulation and to keep the rest of the results in proper context, we first illustrate the well-known kinetics for pure case ( $\epsilon = 0, N_1 = 0\%$ ) at three quench depths in Fig. 1. The evolution morphologies in Fig. 1 are at  $t = 4 \times 10^6$  MCS for (a)  $T = 0.5$ , (b)  $T = 1.0$ , and (c)  $T = 1.5$ , respectively. After a quench, the system evolves with the emergence and growth of domains via SD, showing a typical interconnected, bi-continuous morphology. In the two phases,  $A$ -rich is marked in maroon, and  $B$ -rich is unmarked. At  $T = 0.5$  (deep quench), due to insignificant thermal fluctuations ( $k_B T$ ) in comparison to domain interface energy, coarsening stays in their early stage [1–3] (transient) growth regime of demixing even for MCS  $\mathcal{O}(10^6)$ . However, the system shows typical domain morphologies at higher temperatures:  $T = 1.0$  and  $T = 1.5$ , respectively. The morphology at  $T = 1.5$  (Fig. 1(c)) seems a little fuzzier due to a higher thermal noise than for the other two lower temperatures as in Figs. 1(a)-(b). The insets in Figs. 1(a)-(c) illustrate the spatial intensity variation of the structure factor,  $S(k_x, k_y)$ . The colorbars on the right indicate the range of scattering intensity values for all the temperatures, indicating that the domain evolution for  $T = 0.5$  is in its early stage and faster for  $T = 1.5$ .

To understand the evolution morphology of the pure system at different temperatures, we plot the spherically averaged scaled correlation function,  $C(r, t)$  vs. scaled distance,  $r/\ell(t)$  as displayed in Fig. 1(d). Data sets for  $T = 1.0$  (red curve) and  $T = 1.5$  (green curve) nicely collapse onto a single curve. However, a slight deviation is observed at larger domain sizes ( $r/\ell(t) \in (1,3)$ ) for  $T = 0.5$  (black curve) as domain evolution is still in the transient growth regime. In the inset of Fig. 1(d), we plot the scaled structure factor,  $S(k, t)\ell(t)^{-2}$  vs. scaled distance,  $k\ell(t)$ . Here and in the following  $S(k, t)\ell(t)^{-2}$  vs.  $k\ell(t)$  plots, we have considered the logarithm of data values on both axes, unless stated otherwise. The scaled structure factor curves nicely overlap onto a master curve for higher  $k$  values, i.e., for smaller domain sizes for all the temperatures. Whereas at  $T = 0.5$ ,  $S(k, t)\ell(t)^{-2}$  (denoted by the black circles) deviates from overlapping with the red and green curves for smaller  $k$  values, i.e., larger domain sizes. Therefore, on the time scale of our simulation, the scaling functions demonstrate that the Ising system regards dynamical scaling except for a small deviation for  $T = 0.5$  (deep quench) at smaller  $k$  values. Nevertheless, the large  $k$  region (tail) of the structure factor ( $k \rightarrow \infty$ ) follows Porod's law:  $S(k, t) \sim k^{-3}$ , which results from the scattering of sharp domain interfaces [44,45].

The time-dependence of average domain size ( $\ell(t)$  vs.  $t$  in Fig. 1(e)) illustrate that the evolution kinetics is faster for  $T = 1.0$  (red curve) and  $1.5$  (green curve) than at  $T = 0.5$  (black curve); the former curves follow LS growth law:  $\ell(t) \sim t^{1/3}$  (a well-known diffusive dynamics) [28]. The black curve shows the growth exponent:  $\phi \rightarrow 0.16$ , much smaller than the diffusive growth exponent. To clarify this, we plot the growth exponent,  $\phi_{eff}$  vs.  $1/\ell(t)$  at different temperatures as in the inset Fig. 1(e). At  $T = 1.0$  and  $1.5$ , the growth exponent  $\phi_{eff} \rightarrow 1/3$ . However, for  $T = 0.5$ ,  $\phi_{eff}$  is far from LS growth exponent; this further confirms the slower domain evolution for  $T = 0.5$ . The domain evolution stays in the transient growth regime for the most part of the simulation.

## ii. Low bond-disorder ( $\epsilon = 1$ )

To see the effect of BD introduced in a regular manner, we first examine evolution snapshots at  $t = 4 \times 10^6$  MCS for  $N_1 = 2\%$  in Fig. 2(a)-(c), and  $N_1 = 5\%$  in Fig. 2(d)-(f) quenched at  $T = 0.5$ ,  $1.0$ , and  $1.5$ , respectively. At  $T = 0.5$  (deep quench), much smaller interconnected domains are formed since the surface energy dominates over the thermal energy ( $k_B T$ ). The effect of lower BD ( $N_1 = 2\%$ ,  $5\%$ ) seems to have a minor influence on domain evolution, as demonstrated in Figs. 2(a) and 2(d). When the system is quenched at  $T = 1.0$ , where we usually observe a smooth and bi-continuous domain evolution in the pure case (Fig. 1(b)), shows the formation of short and interconnected stripes oriented in a particular direction as exhibited in Fig. 2(b) and 2(e). Note that the evolution kinetics due to SD is relatively faster for the quench at  $T = 1.5$  (see Fig. 1(c)). Therefore, the short and interconnected stripes formed due to disorder at an early stage of separation kinetics merge to form longer stripes that resemble the fragmented lamellar patterns (see Fig. 2(c) and 2(f)).

The direction of stripe's alignment depends on the number of disordered sites,  $N_1$ . It follows the direction of a higher number of disorder sites [16]. Note that the exchange interaction,  $J_{ij} = 0$  for the disordered sites, which are equivalent to consider the sites at  $T \gg T_c$ . Hence, all the related proposed spin exchanges with nearest-neighbor sites are accepted. Since phase separation kinetics also begins due to the spin-exchange, the most desirable locations for domain evolution would be in the proximities of disordered sites. Therefore, we start noticing the formation of shorter stripes in the direction of a higher number of disordered sites even at early times, leading to more extended stripe patterns at late times.

To compare the effect of lower BD ( $N_1 = 2\%, 5\%$ ) with a pure system, we plot the scaling functions and the effective growth exponents in Figs. 3 and 4, respectively. In Fig. 3(a), we present  $C(r, t)$  vs.  $r/\ell(t)$  plot at  $T = 0.5$  (black curve),  $T = 1.0$  (red curve), and  $T = 1.5$  (green curve) for  $N_1 = 2\%$  at  $t = 4 \times 10^6$  MCS when the system is already in the scaling regime. The corresponding scaled structure factor,  $S(k, t)\ell^{-2}$  vs.  $k\ell$  plot is demonstrated in Fig. 3(b). The data in Figs. 3(a) and 3(b) display a slight deviation from the scaling at larger  $r/\ell(t) \in (1,3)$  after zero-crossing (or smaller  $k\ell(t)$ ) at different temperatures. The extent of deviation from the scaling for  $N_1 = 2\%$  at different temperatures is similar to the one we observed for a pure system (Fig. 1(a)). Nevertheless, a good scaling is observed for most part of the curves.

The characteristic length,  $\ell(t)$  vs.  $t$  plot, is displayed in Fig. 3(c) on a logarithmic scale. Similar to a pure case, the rate of domain size evolution is faster at  $T = 1.0$  (red curve), and 1.5 (green curve) than  $T = 0.5$  (black curve); the system follows LS growth law ( $\phi \rightarrow 1/3$ ) at former temperatures. In contrast, the black curve shows the growth exponent:  $\phi \rightarrow 0.1$ . Figure 3(d) displays the effective growth exponent,  $\phi_{eff}$  against  $1/\ell(t)$  at different temperatures, further suggests the same.

When we increase BD,  $N_1 = 5\%$ , the corresponding scaling functions display a more prominent deviation from the master curve for the larger scaled distances (as displayed in Figs. 4(a) and 4(b) for different temperatures denoted by different symbol types) in compare to  $N_1 = 2\%$  (in Fig. 3). The tail of the structure factor shows a power-law decay:  $S(k, t) \sim k^{-3}$  (Porod's tail) due to scattering from sharp interfaces. The average domain size illustrates the usual LS power-law growth:  $\ell(t) \sim t^{1/3}$  for higher temperatures as depicted in Figs. 4(c) and 4(d) with red ( $T = 1.0$ ) and green ( $T = 1.5$ ) symbols, respectively. However, the growth for  $T = 0.5$  is still the slowest and remains in the transient regime with growth exponent:  $\phi_{eff} \rightarrow 0.05$  (see the inset in Fig. 4(d)).

Interestingly, we notice that at  $T = 0.5$ , the growth exponent,  $\phi_{eff}$  is getting smaller with the increasing BD,  $N_1 = 0\% \rightarrow 5\%$  (see insets in Figs. 1(e), 3(d), and 4(d)). The reason could be the small sizes of domain structures evolved at a low temperature. Since the thermal energy ( $k_B T$ ) of the system is low, the increasing bond-disorder instead of bringing domain evolution out of the early growth stage, it begins to melt the morphologies and hence, the smaller effective growth exponent. On the other hand, the growth law quickly crossover to the diffusive growth regime for shallow quenches:  $\phi_{eff} \rightarrow 1/3$  for all the percentages of BD ( $N_1 = 0\% \rightarrow 5\%$ ) considered here. However, the average domain

size is larger for the higher quench temperature, as demonstrated by the green curves in Figs. 1(e), 3(c), and 4(c), respectively. Although, for  $N_1 = 5\%$ ,  $\phi_{eff}$  crosses over the diffusive growth exponent (1/3) to a higher value at late times. The reason could be the higher  $N_1$  that gradually affects the domain interfaces. Hence, the random motion (diffusion dynamics) of Ising spins set in at the domain boundaries (where the average spin displacement is proportional to  $t^{1/2}$ ) [39] with the phase separation dynamics at late times.

Recall that the morphologies, particularly at  $T = 1.5$ , show long stripes (fragmented lamellar) as displayed in Fig. 2(c) and 2(f) at  $t = 4 \times 10^6$  MCS. Although, the structure factor,  $S(k, t)$  shown in Figs. 3(b) and 4(b) are successfully demonstrating the scaling behavior of the system, but not the induced anisotropy due to stripe morphology because of the spherical averaging of data. For that reason, we plot  $S(k_x, k_y)$  vs.  $k_x$  along the lattice diagonals in Figs. 5(a) and 5(b) for  $N_1 = 2\%$  and  $N_1 = 5\%$ , respectively, to illustrate the same; the black and red curves show the diagonal and cross diagonal structure factors. We average the data over fifty ensembles. The nonoverlapping of curves confirm the presence of structural anisotropy in the system. Notice the switching of black and red curves for  $N_1 = 2\%$  in Fig. 5(a) and  $N_1 = 5\%$  in Fig. 5(b), which demonstrate the change in the stripe's alignment. The corresponding plots of spatial variation of scattering intensity in Figs. 5(c) and 5(d) further verify that the stripe orientation depends on the disorder percentage,  $N_1$ . In addition to that, we observe the similar behavior of  $S(k_x, k_y)$  vs.  $k_x$  plots at  $T = 1.0$  for  $N_1 = 2\%$  and  $N_1 = 5\%$  as shown by the green and blue curves in Figs. 6(a) and 6(b), respectively. However, the plots for  $T = 0.5$ , illustrate an excellent overlap for  $N_1 = 2\%$  and  $N_1 = 5\%$ , as shown by the black and red symbols in Fig. 6, thus sustaining the system's isotropy. Overall, the lower BD has a negligible effect on the scaling functions for the deep quenching. Nonetheless, it influences the scaling functions and length scale of the phase separating system more when shallow quenched.

### iii. High bond-disorder ( $\epsilon = 1$ )

Next, we introduce  $N_1 = 10\%$  BD at regularly selected sites in the system. Figure 7 shows the corresponding evolution morphology at  $T = 0.5$  (in Figs. 7(a)-(c)),  $T = 1.0$  (in Figs. 7(d)-(f)), and  $T = 1.5$  (in Figs. 7(g)-(i)) for  $t = 1 \times 10^6$ ,  $t = 2 \times 10^6$ , and  $t = 4 \times 10^6$  MCS, respectively. Notice the patterns at  $T = 0.5$  for which we observe a much slower domain evolution where the system's isotropy is preserved for  $N_1 = 2\%$ , and  $5\%$ ; in this case, the evolving domains begin to form stripes, oriented along the direction of effectively higher BD. The stripe patterns evolve into a fragmented lamellar at  $t = 1 \times 10^6$

(Figs. 7(a)). The broken lamellar evolves further to form a perfect lamellar at a late time,  $t = 4 \times 10^6$  (Figs. 7(c)). Thus, when the system is deep quenched,  $N_1 = 10\%$  BD seems sufficient to bring the growth kinetics out of the transient regime, and hence, domains begin to evolve into the stripe morphologies. A few tiny random domains of *A*-type (marked in maroon) are seen in the *B*-type phases (unmarked) in Fig. 7. The fuzziness in the system is due to the larger thermal fluctuation (noise) for  $N_1 = 10\%$ . At a lower BD, we observe broken lamellar structures for the higher temperature even at a very late time ( $t = 4 \times 10^6$ ). However, for  $N_1 = 10\%$ , we get similar morphologies much earlier, which form the perfect lamellar patterns at late times. Therefore, when 10% BD is introduced in the system, anisotropic structures develop as time goes on for all the quench temperatures ( $T < T_c$ ) discussed here.

To understand the evolutionary morphology depicted in Fig. 7, we first present the scaling functions for  $T = 1.0$ . In Fig. 8(a), we plot the spherically averaged, scaled correlation function,  $C(r, t)$  vs.  $r/\ell(t)$  at three different times during the evolution as denoted by various symbols. The morphology at  $t = 1 \times 10^6$ , from fragmented long stripes, transformed to an ordered lamellar pattern at  $t = 4 \times 10^6$  (see Fig. 7(d)-(f)), the corresponding  $C(r, t)$  data sets show deviation from the dynamical scaling. The scaled structure factor data sets (in Fig. 8(b)) also manifest the same as time goes on. The structure factor tail deviates from Porod's power-law decay at late times as  $k \rightarrow \infty$  (shown by the red and green curves). Note that Porod's law [44,45] results from the scattering off sharp domain interfaces of small domain structures. However, due to the enhanced thermal noise at a higher BD, the sharp domain interfaces become fuzzier and hence, the deviation from well-known Porod's law. Over time, the main peak of the structure factor gets narrower for smaller  $k$  values. For larger  $k$  values,  $S(k, t)$  begins to show oscillatory behavior (shown in Fig. 8(b) by the red and green symbols) that characterizes the periodicity developed in the system due to lamellar patterns.

Figure 8(c) demonstrates that the average domain size,  $\ell(t)$  follows the usual LS growth law  $\ell(t) \sim t^{1/3}$  for initial time steps; the solid black line shows the expected growth exponent,  $\phi = 1/3$ . Later, as time goes beyond  $t \approx 0.5 \times 10^6$ , we observe a gradual crossover to  $\ell(t) \sim t^{1/2}$  growth law. A higher disorder causes the random motion (the average displacement of a random particle  $\sim t^{1/2}$ ) of spins at domain interfaces that sets in with the phase separation dynamics, and hence the crossover to higher growth exponent:  $\phi \sim 1/2$ . For  $t > 1.7 \times 10^6$ , the growth law interestingly crosses over to a saturation regime, which shows

no further domain growth in the system. Hence, the evolved lamellar morphologies are frozen. To justify it further, we estimate the effective growth exponent,  $\phi_{eff}$  and plot it against  $\ell(t)^{-1}$  as shown in the inset of Fig. 8(c). The curve displays  $\phi_{eff} \rightarrow 1/3$  for the smaller  $\ell(t)$  in a short period, and for an intermediate time interval,  $\phi_{eff} \rightarrow 1/2$ ; however, in the asymptotic limit  $\phi_{eff} \rightarrow 0$  as  $\ell(t)^{-1} \rightarrow 0$ .

To identify the anisotropy induced in the system due to lamellar morphology, we plot the structure factor,  $S(k_x, k_y)$  vs.  $k_x$  along the lattice diagonals in Fig. 8(d) for the evolution shown in Figs. 7(d)-(f)). The black and red curves represent  $S(k_x, k_y)$  for  $t = 1 \times 10^6$  MCS along the positive diagonal (diagonal dexter: normal to the stripes). The green and blue curves display the same for  $t = 4 \times 10^6$  MCS along with the cross-diagonal (diagonal sinister: along with the stripes). The structure factor along the diagonal dexter maintains a high amplitude peak (black and green curves), whereas the peaks along the cross-diagonals (red and blue curves) remain very low. Hence, the nonoverlapping of curves along the diagonals confirm the anisotropy in the system. Over time, we observe the formation of another peak in  $S(k_x, k_y)$  at large  $k_x$ , which shows the formation of secondary structure in the system. Note that  $S(k_x, k_y)$  is averaged over fifty ensembles (not spherically averaged) for better statistics. The spatial variation of scattering intensity at  $t = 1 \times 10^6$ ,  $2 \times 10^6$ , and  $4 \times 10^6$  MCS as plotted in Figs. 8(e)-(g) further demonstrate the system's anisotropy.

Recall that the effect of lower BD ( $N_1 = 2\%$ ,  $5\%$ ) was more significant on the evolution kinetics for the shallow quenched temperature. Next, to see the impact of quench depth for  $N_1 = 10\%$ , we compare the scaling functions and length scales in the asymptotic time limit,  $t = 4 \times 10^6$  MCS for three different temperatures:  $T = 0.5$ ,  $1.0$ , and  $1.5$  in Fig. 9. The data sets for  $C(r, t)$  vs.  $r/\ell(t)$  and  $S(k, t)\ell(t)^{-2}$  vs.  $k\ell(t)$  do not overlap as demonstrated in Fig. 9(a) and 9(b), respectively, by the black ( $T = 0.5$ ), red ( $T = 1.0$ ), and green ( $T = 1.5$ ) symbols. The deviation from the scaling ensures that the evolved morphologies do not belong to the same universality class. The solid black line with slope  $= -3$  in Fig. 9(b) shows the deviation of the structure factor from Porod's law for  $k \rightarrow \infty$ . The oscillations in  $S(k, t)\ell(t)^{-2}$  vs.  $k\ell(t)$ ) curves confirm the periodicity in the system due to lamellar morphology.

The characteristic length scale follows LS growth law ( $\phi \sim 1/3$ ) at early times for all the temperatures indicated in Fig. 9(c). During the intermediate time, the growth law gradually crossover to diffusion kinetics ( $\phi \sim 1/2$ ) due to the random motion of spins at

domain interfaces at higher BD. Beyond  $t > 10^6$  MCS, the domain growth freezes to a finite value at higher temperatures (see the red and green curves at  $T = 1.0$  and  $1.5$ , respectively). The system attains its equilibrium lamellar morphology earlier for  $T = 1.5$ , which is evident as the growth kinetics is relatively faster at higher temperatures; the evolution patterns in Figs. 5(g)-5(i) also confirm the same. We plot  $S(k_x, k_y)$  vs.  $k_x$  along the diagonals in Fig. 9(d) to illustrate the anisotropy in the system due to lamellar morphology. For  $T = 0.5$ , the black and red curves and for  $T = 1.5$ , the green and blue curves show the  $S(k_x, k_y)$  along the diagonal dexter and diagonal sinister of the lattice, respectively. The structure factor peak normal to the stripes (for the diagonal dexter) retains much higher amplitude than along the strips (diagonal sinister). Thus the nonoverlapping of  $S(k_x, k_y)$  vs.  $k_x$  curves demonstrate the presence of anisotropy in the system.

Overall, our results suggest that for the lower bond disorders ( $N_1 = 2\%$  and  $5\%$ ) at  $T = 0.5$ , the scaling function data (the spherically averaged correlation function and the structure factor) collapse neatly onto the scaling function of a pure system ( $N_1 = 0\%$ ) as demonstrated in Figs. 10(a) and 10(b), with black, red, and green symbols for  $t = 4 \times 10^6$  MCS. Therefore, the system with  $N_1 = 0\%$ ,  $2\%$ , and  $5\%$  BD quenched at  $T = 0.5$  belong to the same dynamical universality class. In other words, the morphologies are statistically similar to the pure morphology when evolved at  $T = 0.5$ . The symmetry in the scattering intensity variation for  $N_1 = 2\%$  (in Fig. 10(c)) and  $N_1 = 5\%$  (in Fig. 10(d)) further justify the isotropy of evolved  $A$  and  $B$  phases within a negligible deviation with the pure case (in Fig. 1(a)). Hence, they belong to the same dynamical universality class. However, for  $N_1 = 10\%$ , the morphology of  $A$  and  $B$  phases transformed into lamellar patterns. Hence, the deviation from the dynamical scaling function (indicated by the blue symbols in Figs. 10(a)-(b)) shows that system does not belong to the same universality class. The scattering intensity variation in Fig. 10(e) manifests the same. Recall that when the system is quenched at  $T = 1.0$  or  $1.5$ , the anisotropy was induced in the system even at a lower BD ( $N_1 = 2\%$ , and  $5\%$ ) in the form of short/long stripe patterns (see Figs. 2 - 6). Whereas, when BD is increased up to  $N_1 = 10\%$ , the strips transform into a broken lamellar pattern which becomes a perfect lamellar at late times for all the quench temperatures.

#### 4. Summary and conclusion

We studied the phase separation kinetics of the critical binary ( $AB$ ) mixture extensively under the influence of BD, introduced in a regular manner by utilizing the Monte Carlo (MC)

simulation technique at different quench depths. The separation kinetics was modeled using the conserved (Kawasaki) spin-exchange dynamics on the  $2d$  Ising model. The coupling strength for a site  $i$  with its nearest neighbor ( $nn$ ) site  $j$  was defined as  $J_{ij} = 1 - \epsilon_{ij}$  where we set  $\epsilon_{ij} = 1$  for the disorder site and  $\epsilon_{ij} = 0$  for the remaining sites. In particular, we explored the influence of several percentages of BD:  $N_1 = 0\%$  (pure case) 2%, 5%, and 10%, and quench depths:  $T = 0.5, 1.0$ , and  $1.5$  on the characteristic features of phase separation kinetics such as the evolution morphology, the scaling functions, and the growth law.

We found that when the homogeneous binary mixture was deeply quenched at  $T = 0.5$ , the influence of lower BD,  $N_1 = 2\%$  and  $5\%$  on the segregation kinetics was negligible. The system showed an excellent dynamical scaling with the pure case ( $N_1 = 0\%$ ), displayed by the scaled correlation function,  $C(r, t)$ , and the structure factor,  $S(k, t)$  at a given time step. The domain evolution stayed in the transient growth regime even in the asymptotic time limit ( $t = 4 \times 10^6$  MCS). The effective growth exponent,  $\phi_{eff} \sim 0.16$  for the pure case, decreased even further,  $\phi_{eff} \sim 0.05$  for  $N_1 = 5\%$  due to randomness at domain interfaces caused by the disorder. Thus, the domain growth exponent for a binary mixture quenched at  $T = 0.5$  and for lower BD,  $N_1 = 0\%, 2\%$ , and  $5\%$  were much smaller than the usual *Lifshitz-Slyozov* (LS) growth exponent,  $\phi_{eff} \sim 1/3$ .

On the other hand, when the system was quenched at higher temperatures:  $T = 1.0$ , and  $T = 1.5$ , the effect of lower BD:  $N_1 = 2\%$  and  $5\%$  was visible on the evolution kinetics. For a pure case ( $N_1 = 0\%$ ), the system displayed the expected evolution kinetics. For  $N_1 = 2\%$  and  $5\%$  BD, the system evolved to form the short and interconnected stripe patterns at  $T = 1.0$ ; however, the long and fragmented lamellar morphology was observed at  $T = 1.5$ . These morphologies were oriented particularly in the direction of a higher number of disorder sites. Thus, the evolved domains developed into anisotropic morphologies and hence the deviation from the dynamic scaling. The variation becomes more noticeable with the increase in BD at higher quench temperatures. However, the growth law was essentially consistent with LS power-law growth.

When BD was set to  $N_1 = 10\%$ , we observed the formation of long fragmented strips at early times for all the temperatures studied here. These stripe patterns gradually transformed into a perfect lamellar morphology at late times. Thus, the system showed a significant deviation from the dynamical scaling for different times at a given temperature and also at various temperatures for a fixed time. The domain growth was initially consistent with LS growth-law:  $\phi_{eff} \sim 1/3$ , which gradually crossed over to the diffusion

dynamics (random motion of particles):  $\phi_{eff} \sim 1/2$  during the intermediate time. However, on the time scale of our simulation, the domain growth was frozen to a finite size when the system is believed to form its equilibrium (stable) lamellar morphology. The domain growth at  $T = 1.5$  reached saturation earlier than at  $T = 1.0$ . Nevertheless, we have not accessed the saturation in the growth kinetics for  $T = 0.5$ ; however, there is a possibility to access the same at a much later time than investigated here.

In general, pattern formation in the disordered system is of great technological importance. Our model can be integrated to understand a wide variety of physical phenomena such as structural evolution in the biological system (e.g., the iridescent color patterns of bird feathers observed due to refraction of incident light from the phase-separated frozen nanostructures), self-organizing spatial patterns in ecological systems (e.g., mussel beds, etc.). The phase separation kinetics in multiphase fluid and mineral exsolution can also be easily explained. Finally, our simulation results provide a general framework for the experiments on domain growth in Ising systems with BD. In the future, we aim to address the effect of BD and quench depths for the Ising systems in  $3d$  where similar experiments have not yet been performed. Thus, we hope our simulation results will certainly offer the essential guidelines for future studies.

### Conflicts of interest

There are no conflicts of interest to declare.

### Acknowledgments

S. S. would like to acknowledge IIT (BHU) for financial support. In addition, A. S. acknowledges the financial support from SERB Grant No. ECR/2017/002529 by the Department of Science and Technology, New Delhi, India.

### References

- [1] S. Puri and V. K. Wadhawan, *Kinetics of Phase Transitions* (CRC Press, Boca Raton, FL, 2009).
- [2] A. J. Bray, *Theory of Phase-Ordering Kinetics*, *Advances in Physics* **43**, 357 (1994).
- [3] A. Onuki, *Phase Transition Dynamics* (2002).
- [4] K. Binder and P. Fratzl, *Spinodal Decomposition*, in *Materials Science and Technology* (Wiley-VCH Verlag GmbH & Co. KGaA, Weinheim, Germany, 2013).
- [5] R. A. L. Jones, *Soft Condensed Matter* (Oxford University Press, Oxford, 2008).
- [6] H. Ikeda, Y. Endoh, and S. Itoh, *Ordering Kinetics in a Two-Dimensional Percolation Magnet*, *Physical Review Letters* **64**, 1266 (1990).
- [7] V. Likodimos, M. Labardi, and M. Allegrini, *Kinetics of Ferroelectric Domains Investigated by Scanning Force Microscopy*, *Physical Review B* **61**, 14440 (2000).

- [8] V. Likodimos, M. Labardi, X. K. Orlik, L. Pardi, M. Allegrini, S. Emonin, and O. Marti, *Thermally Activated Ferroelectric Domain Growth Due to Random Defects*, Physical Review B **63**, 064104 (2001).
- [9] A. J. Bray and K. Humayun, *Universality Class for Domain Growth in Random Magnets*, Journal of Physics A: Mathematical and General **24**, L1185 (1991).
- [10] D. J. Srolovitz and G. S. Grest, *Impurity Effects on Domain-Growth Kinetics. II. Potts Model*, Physical Review B **32**, 3021 (1985).
- [11] G. S. Grest and D. J. Srolovitz, *Impurity Effects on Domain-Growth Kinetics. I. Ising Model*, Physical Review B **32**, 3014 (1985).
- [12] J. H. Oh and D.-I. Choi, *Monte Carlo Study of the Domain Kinetics of the Ising Model with Random Coupling Constants*, Physical Review B **33**, 3448 (1986).
- [13] D. Chowdhury, M. Grant, and J. D. Gunton, *Interface Roughening and Domain Growth in the Dilute Ising Model*, Physical Review B **35**, 6792 (1987).
- [14] M. F. Gyure, S. T. Harrington, R. Strilka, and H. E. Stanley, *Scaling in Late Stage Spinodal Decomposition with Quenched Disorder*, Physical Review E **52**, 4632 (1995).
- [15] A. Singh, A. Mukherjee, H. M. Vermeulen, G. T. Barkema, and S. Puri, *Control of Structure Formation in Phase-Separating Systems*, Journal of Chemical Physics **134**, 044910 (2011).
- [16] A. Singh, A. Singh, and A. Chakraborti, *Effect of Bond-Disorder on the Phase-Separation Kinetics of Binary Mixtures: A Monte Carlo Simulation Study*, Journal of Chemical Physics **147**, 124902 (2017).
- [17] S. Majumder, S. K. Das, and W. Janke, *Universal Finite-Size Scaling Function for Kinetics of Phase Separation in Mixtures with Varying Number of Components*, Physical Review E **98**, 042142 (2018).
- [18] R. Agrawal, M. Kumar, and S. Puri, *Domain Growth and Aging in the Random Field X Y Model: A Monte Carlo Study*, Physical Review E **104**, 044123 (2021).
- [19] M. Tateno and H. Tanaka, *Power-Law Coarsening in Network-Forming Phase Separation Governed by Mechanical Relaxation*, Nature Communications 2021 12:1 **12**, 1 (2021).
- [20] H. Manzanarez, J. P. Mericq, P. Guenoun, and D. Bouyer, *Modeling the Interplay between Solvent Evaporation and Phase Separation Dynamics during Membrane*, Journal of Membrane Science **620**, 118941 (2021).
- [21] K. Takae and H. Tanaka, *Role of Hydrodynamics in Liquid-Liquid Transition of a Single-Component Substance*, Proceedings of the National Academy of Sciences of the United States of America **117**, 4471 (2020).
- [22] J. Fan, T. Han, and M. Haataja, *Hydrodynamic Effects on Spinodal Decomposition Kinetics in Planar Lipid Bilayer Membranes*, The Journal of Chemical Physics **133**, 235101 (2010).
- [23] R. Paul, S. Puri, and H. Rieger, *Domain Growth in Ising Systems with Quenched Disorder*, Physical Review E **71**, 061109 (2005).
- [24] R. Paul, S. Puri, and H. Rieger, *Domain Growth in Random Magnets*, Europhysics Letters (EPL) **68**, 881 (2004).

- [25] S. Puri and N. Parekh, *Non-Algebraic Domain Growth in Binary Alloys with Quenched Disorder*, Journal of Physics A: Mathematical and General **25**, 4127 (1992).
- [26] S. Puri, D. Chowdhury, and N. Parekh, *Non-Algebraic Domain Growth in Random Magnets: A Cell Dynamical Approach*, Journal of Physics A: Mathematical and General **24**, L1087 (1991).
- [27] D. A. Huse and C. L. Henley, *Pinning and Roughening of Domain Walls in Ising Systems Due to Random Impurities*, Physical Review Letters **54**, 2708 (1985).
- [28] I. M. Lifshitz and V. V. Slyozov, *The Kinetics of Precipitation from Supersaturated Solid Solutions*, Journal of Physics and Chemistry of Solids **19**, 35 (1961).
- [29] A. Singh, S. Puri, and C. Dasgupta, *Kinetics of Phase Separation in Polymer Mixtures: A Molecular Dynamics Study*, The Journal of Chemical Physics **140**, 244906 (2014).
- [30] T. Koga and K. Kawasaki, *Spinodal Decomposition in Binary Fluids: Effects of Hydrodynamic Interactions*, Physical Review A **44**, R817 (1991).
- [31] V. M. Kendon, J.-C. Desplat, P. Bladon, and M. E. Cates, *3D Spinodal Decomposition in the Inertial Regime*, Physical Review Letters **83**, 576 (1999).
- [32] T. Nattermann and J. Villain, *Random-field Ising Systems: A Survey of Current Theoretical Views*, Phase Transitions **11**, 5 (1988).
- [33] A. J. Bray and M. A. Moore, *Scaling Theory of the Random-Field Ising Model*, Journal of Physics C: Solid State Physics **18**, L927 (1985).
- [34] M. Kumar, V. Banerjee, and S. Puri, *Random Field Ising Model with Conserved Kinetics: Super-Universality Violation, Logarithmic Growth Law and the Generalized Tomita Sum Rule*, EPL **117**, (2017).
- [35] V. Likhoshesterov, Y. Maximov, M. Chertkov, L. Vidmar, M. Rigol, I. Balog, G. Tarjus, M. Tissier, A. Bupathy, M. Kumar, V. Banerjee, and S. Puri, *Random Field Ising Models: Fractal Interfaces and Their Implications*, Journal of Physics: Conference Series **905**, 012025 (2017).
- [36] L. Onsager, *Crystal Statistics. I. A Two-Dimensional Model with an Order-Disorder Transition*, Physical Review **65**, 117 (1944).
- [37] A. Singh, *Kinetics of Domain Growth in Ising Systems with Bond Disorder at Regularly Selected Sites*, Bulletin of Materials Science 2020 43:1 **43**, 1 (2020).
- [38] M. E. J. Newman and G. T. Barkema, *Monte Carlo Methods in Statistical Physics* (Oxford University Press, Oxford, UK, 1999).
- [39] D. P. Landau and K. Binder, *A Guide to Monte Carlo Simulations in Statistical Physics*, 4th edition (Cambridge University Press, Cambridge, Massachusetts, 2014).
- [40] S. Puri and H. L. Frisch, *Phase Separation in Binary Mixtures with Chemical Reactions*, International Journal of Modern Physics B **12**, 1623 (1998).
- [41] Y. Oono and S. Puri, *Computationally Efficient Modeling of Ordering of Quenched Phases*, Physical Review Letters **58**, 836 (1987).
- [42] A. Chakrabarti, R. Toral, and J. D. Gunton, *Late Stages of Spinodal Decomposition in a Three-Dimensional Model System*, Physical Review B **39**, 4386 (1989).

- [43] S. Majumder and S. K. Das, *Temperature and Composition Dependence of Kinetics of Phase Separation in Solid Binary Mixtures*, Physical Chemistry Chemical Physics **15**, 13209 (2013).
- [44] G. Porod, *Small Angle X-Ray Scattering*, in *Small Angle X-Ray Scattering*, edited by O. Glatter and O. Kratky (Academic Press, New York, 1982).
- [45] Y. Oono and S. Puri, *Large Wave Number Features of from Factors for Phase Transition Kinetics*, Modern Physics Letters B **02**, 861 (1988).

## Figures

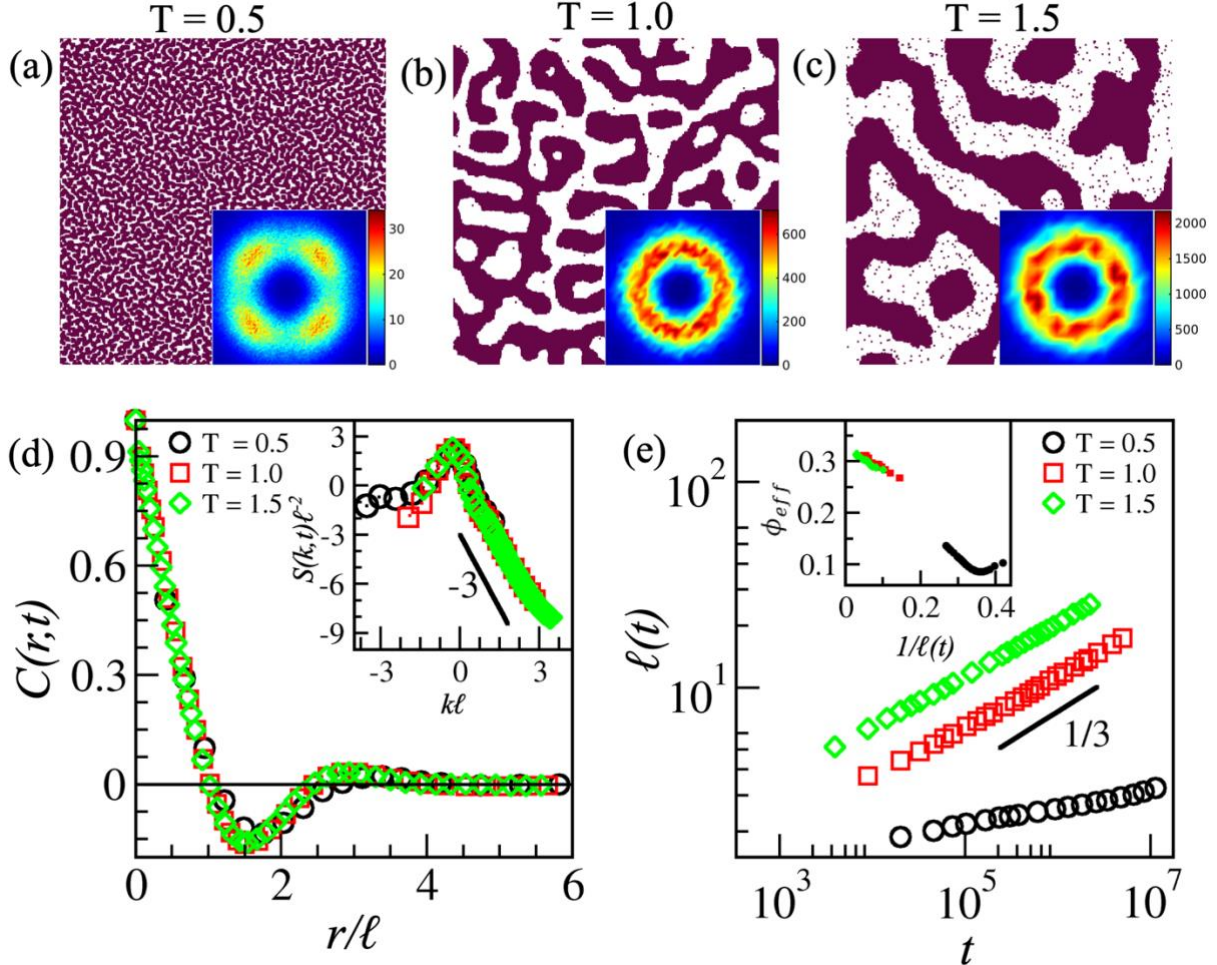


Figure 1: (a) Evolution snapshots of a pure ( $N_1 = 0\%$ ) critical binary ( $AB$ ) mixture at  $t = 4 \times 10^6$  MCS for (a)  $T = 0.5$ , (b)  $T = 1.0$ , and (c)  $T = 1.5$ . The insets in Figs. (a)-(c) illustrate the spatial intensity variation of the structure factor,  $S(k_x, k_y)$ . (d) The scaling plot of  $C(r, t)$  vs.  $r / \ell(t)$ ; data sets at  $T = 0.5$ ,  $1.0$ , and  $1.5$  collapse nicely onto a single curve. The inset shows the plot of scaled structure factor,  $S(k, t) \ell(t)^{-2}$  vs.  $k \ell(t)$ . The structure factor tail follows Porod's law,  $S(k, t) \sim k^{-3}$  for  $k \rightarrow \infty$ . (e) The log-log plot of the characteristic length scale  $\ell(t)$  vs.  $t$  for the evolution shown in (a)-(c). The solid black line shows the expected growth exponent,  $\phi = 1/3$  for the pure case; the inset plot shows the variation of effective growth exponent,  $\phi_{eff}$  as a function of  $1/\ell(t)$ .

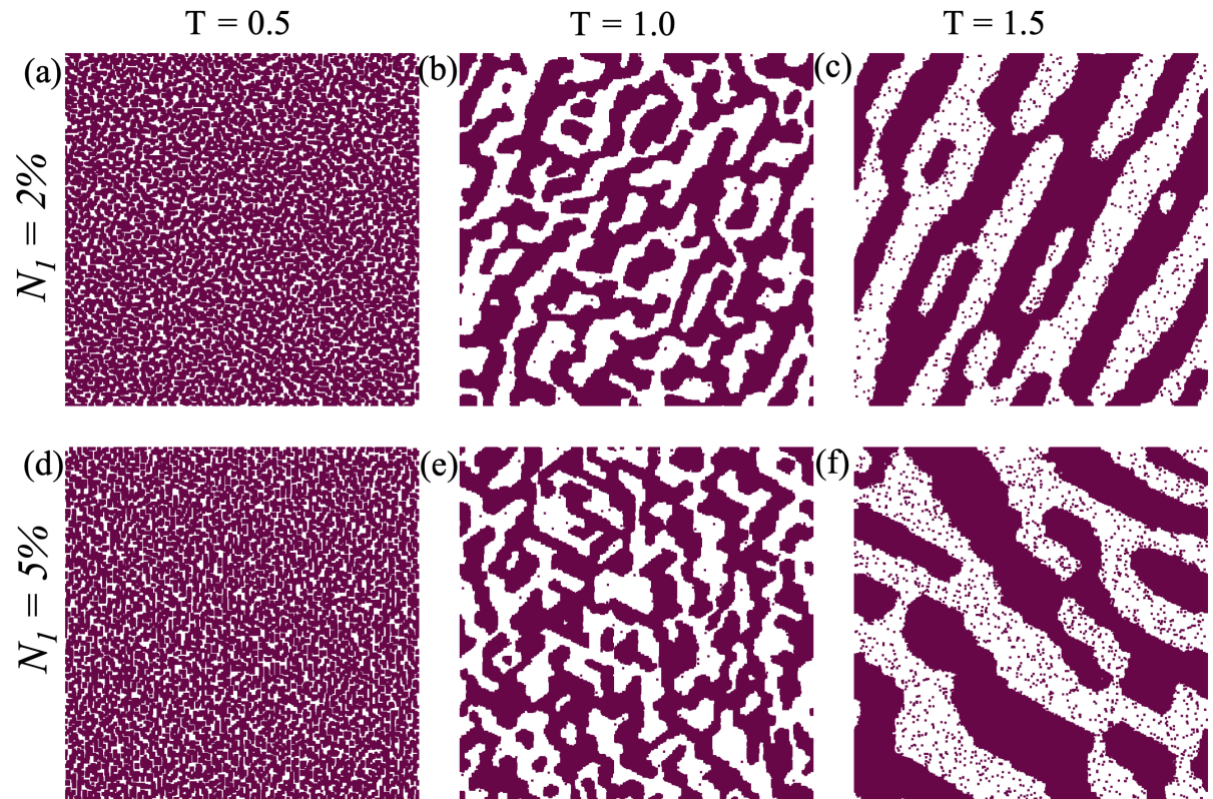


Figure 2: (a) Evolution snapshots for  $N_1 = 2\%$ , and  $5\%$  at  $t = 4 \times 10^6$  MCS for  $T = 0.5, 1.0$  and  $1.5$ , respectively.

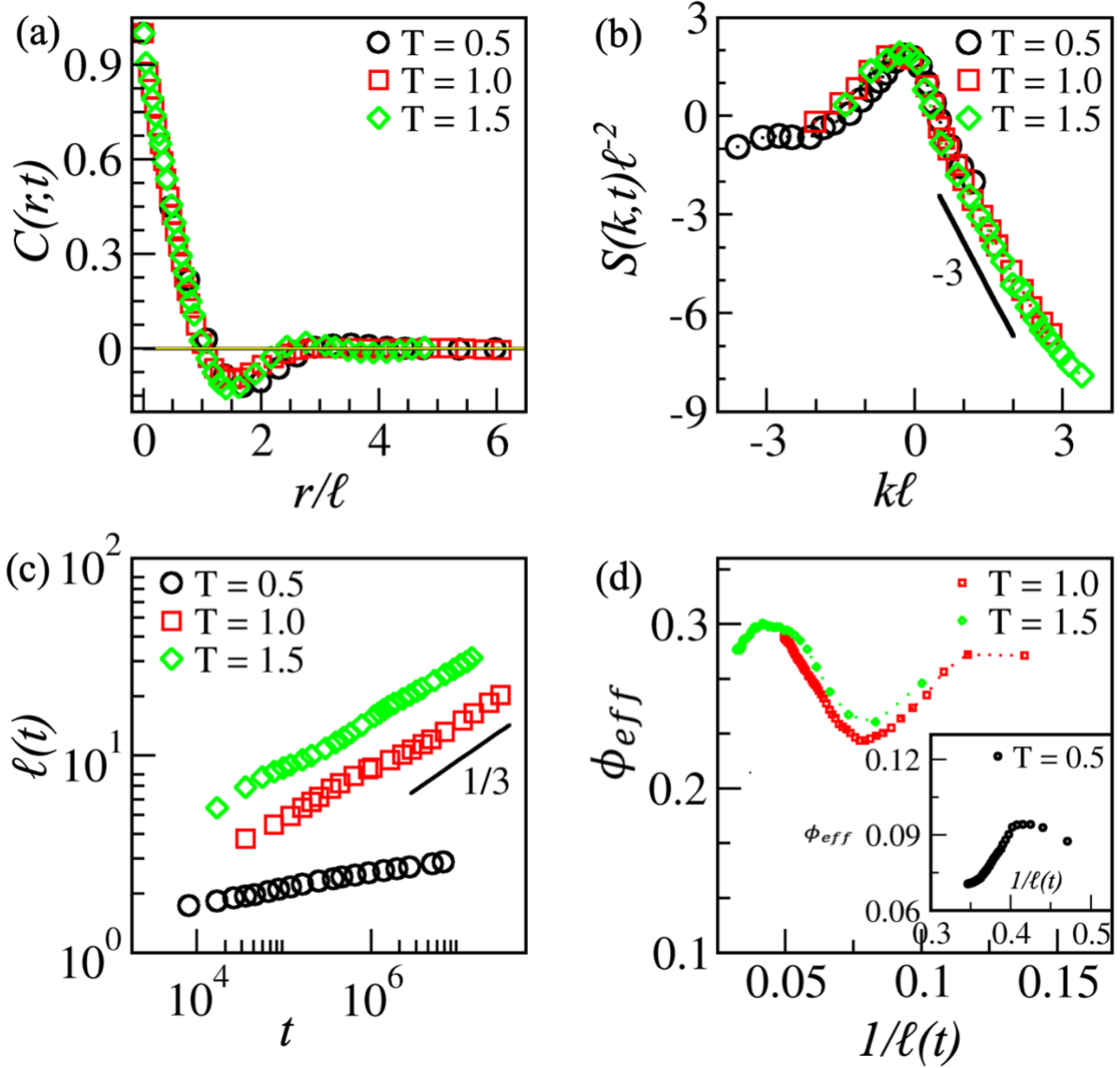


Figure 3: Scaling plot of  $C(r, t)$  vs.  $r/\ell(t)$  in (a), and  $S(k, t)\ell(t)^{-2}$  vs.  $k\ell(t)$  in (b) for  $N_1 = 2\%$  of bond disorder at three quench temperatures as indicated by the different symbols. (c) Log-log plot of length scale,  $\ell(t)$  vs.  $t$ , and (d) effective growth exponent,  $\phi_{eff}$  vs.  $1/\ell(t)$  corresponding to the length scale shown in Fig. (c) at  $T = 1.0$  and  $1.5$ . The inset in (d) shows  $\phi_{eff}$  for  $T = 0.5$ .

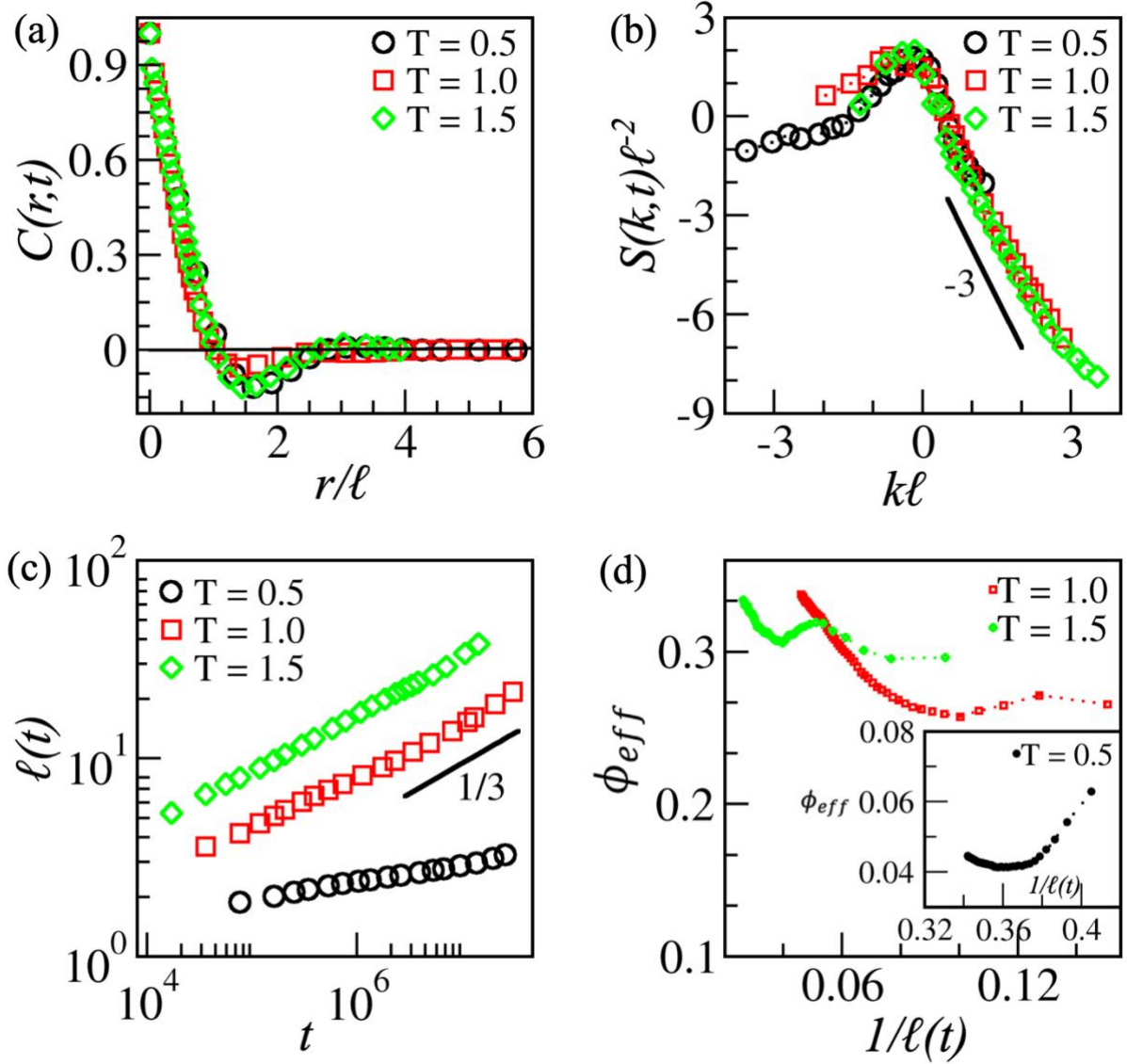


Figure 4: Scaling plots of  $C(r,t)$  vs.  $r/\ell(t)$  for  $N_1 = 5\%$  in (a) and  $S(k,t)\ell(t)^{-2}$  vs.  $k\ell(t)$  in (b) at different temperatures shown by the different symbol types. (c) Log-log plot of length scale,  $\ell(t)$  vs.  $t$ . (d) The effective growth exponent,  $\phi_{eff}$  vs.  $1/\ell(t)$  corresponding to data in Figs. 2(e)-(f). The inset in (d) shows  $\phi_{eff}$  vs.  $1/\ell(t)$  for  $T = 0.5$ .

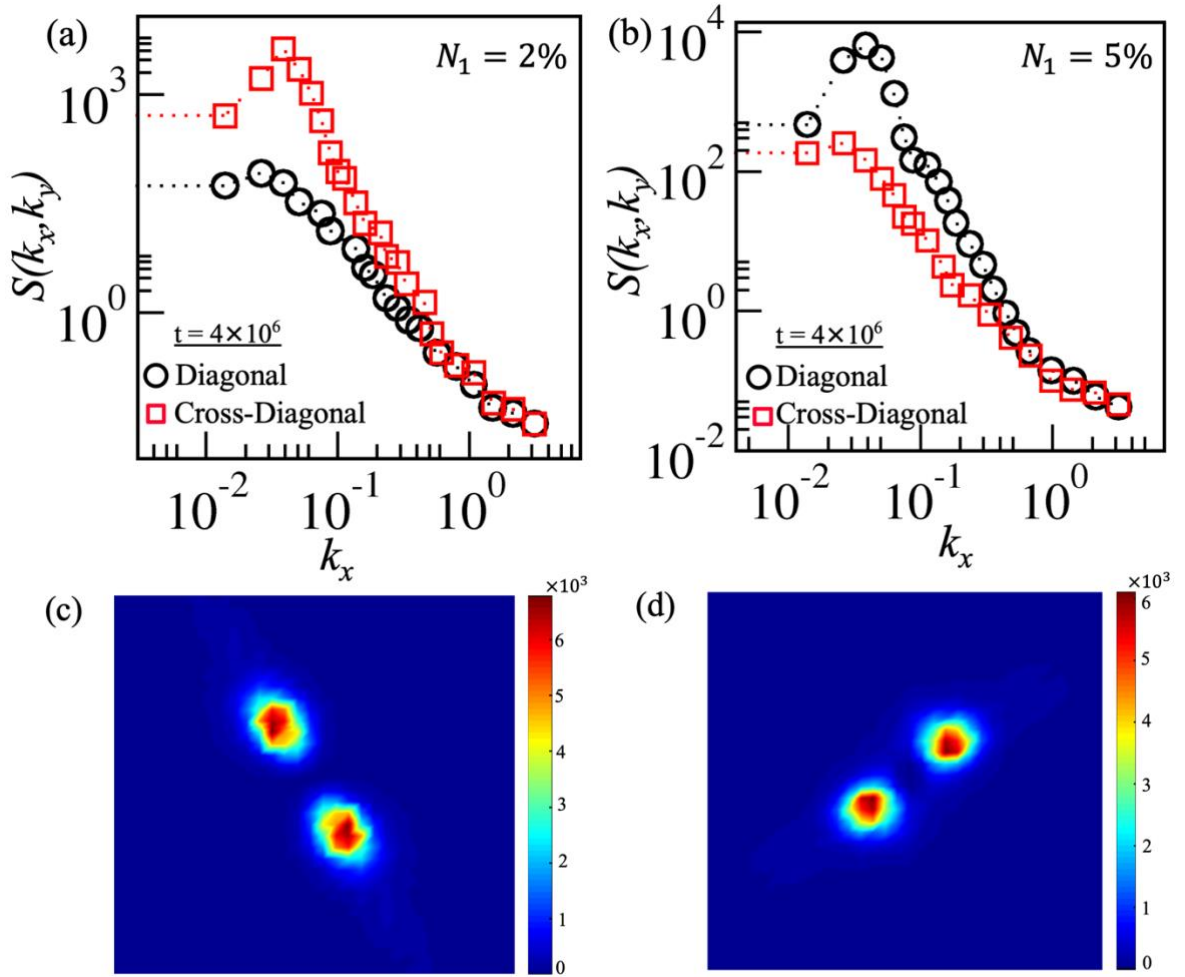


Figure 5: Plots of  $S(k_x, k_y)$  along the lattice diagonals at  $t = 4 \times 10^6$  MCS for (a)  $N_1 = 2\%$ , and (b)  $N_1 = 5\%$ , respectively at  $T = 1.5$ . (c)-(d) shows the spatial intensity variation of the structure factor,  $S(k_x, k_y)$  for  $t = 4 \times 10^6$  MCS.

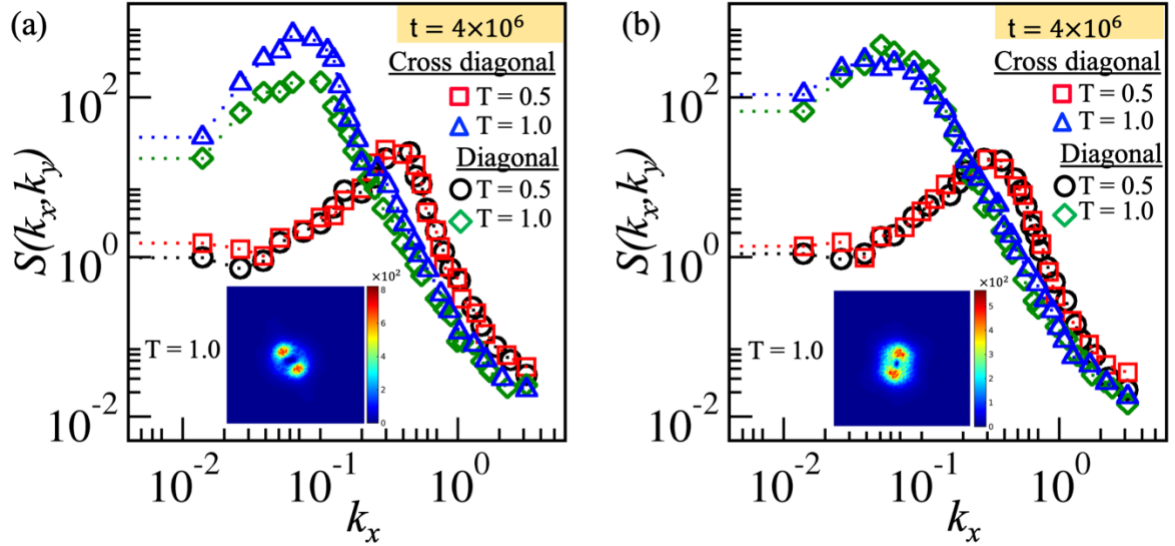


Figure 6: (a) Plot of  $S(k_x, k_y)$  vs.  $k_x$  across the lattice diagonals for  $N_1 = 2\%$  at  $T = 0.5$  (black and red curves), and  $T = 1.0$  (green and blue curves) at  $t = 4 \times 10^6$  MCS. (b) Shows the same as in (a) for  $N_1 = 5\%$ . The insets (a) and (b) display the spatial scattering intensity variation at  $T = 1.0$  for  $N_1 = 2\%$  and  $5\%$ .

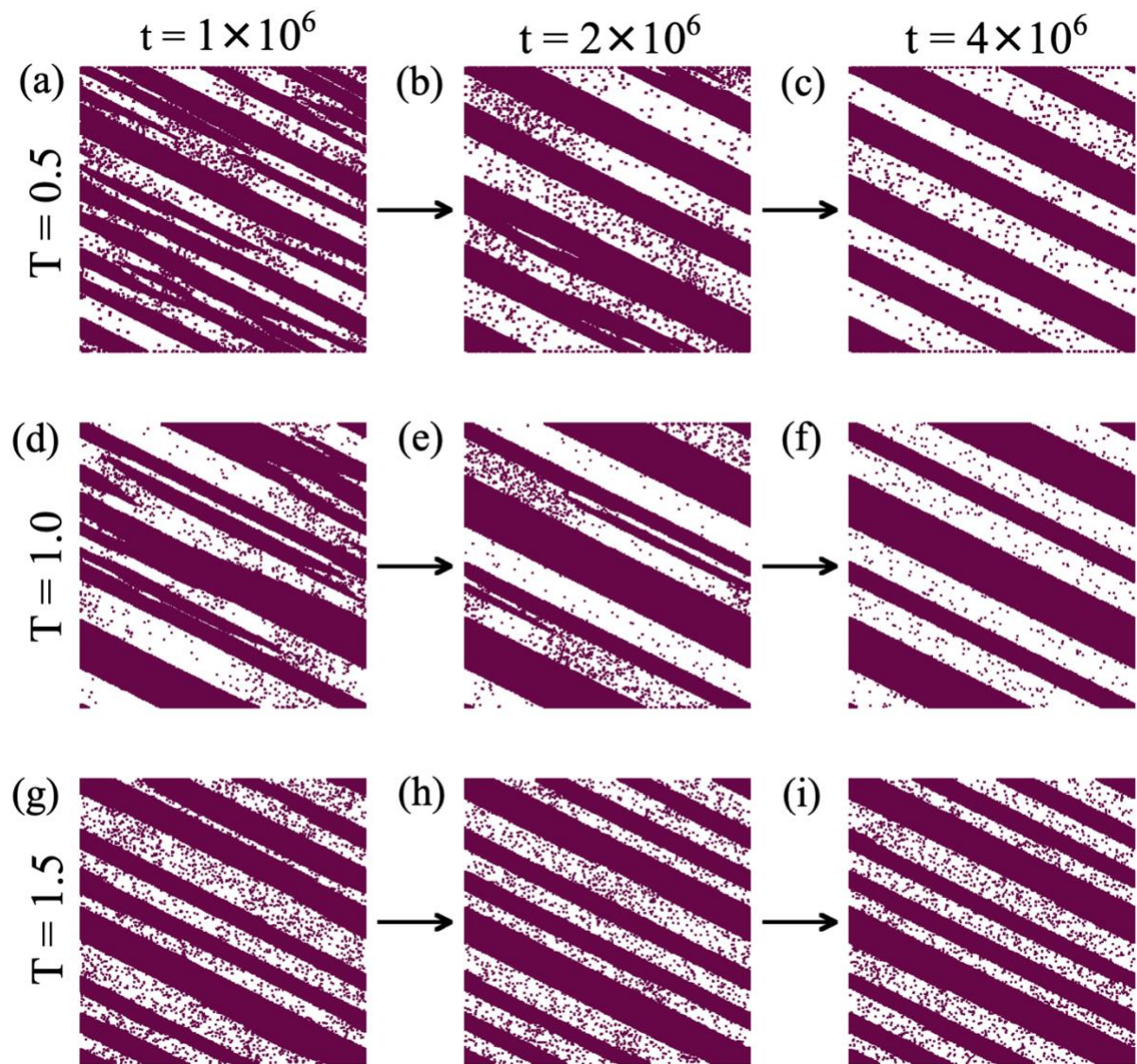


Figure 7: Evolution snapshots at  $t = 1 \times 10^6$ ,  $2 \times 10^6$ , and  $4 \times 10^6$  MCS for  $T = 0.5$ ,  $1.0$ , and  $1.5$ , respectively at  $N_1 = 10\%$  of bond disorder.

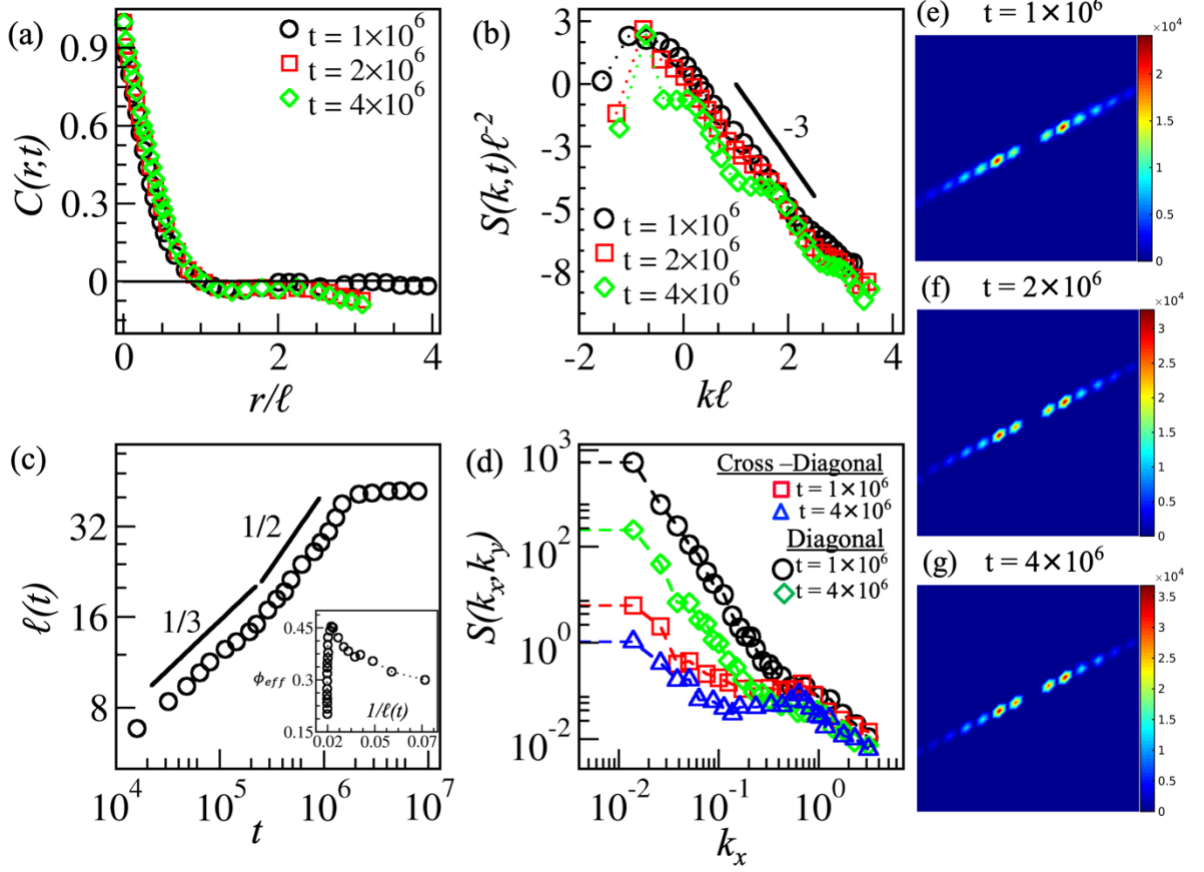


Figure 8: Plot of the scaling functions and the length scale for  $N_1 = 10\%$  at  $T = 1.0$ . (a)  $C(r,t)$  vs.  $r/\ell(t)$  for the evolutions shown in Figs. 7(d)-(f) at  $t = 1 \times 10^6$ ,  $2 \times 10^6$ , and  $4 \times 10^6$ , respectively. (b) Plot of  $S(k,t)\ell(t)^{-2}$  vs.  $k\ell(t)$  corresponding to data sets in (a). (c) The characteristic length scale,  $\ell(t)$  vs.  $t$  on the log-log scale; inset shows the effective growth exponent,  $\phi_{eff}$  vs.  $\ell(t)^{-1}$ . (d) Structure factor,  $S(k_x, k_y)$  vs.  $k_x$  along the lattice diagonals for the evolution at  $t = 1 \times 10^6$  and  $t = 4 \times 10^6$  MCS. (e)-(g) The plot of spatial variation of scattering intensity for  $t = 1 \times 10^6$ ,  $2 \times 10^6$  and  $4 \times 10^6$  MCS.

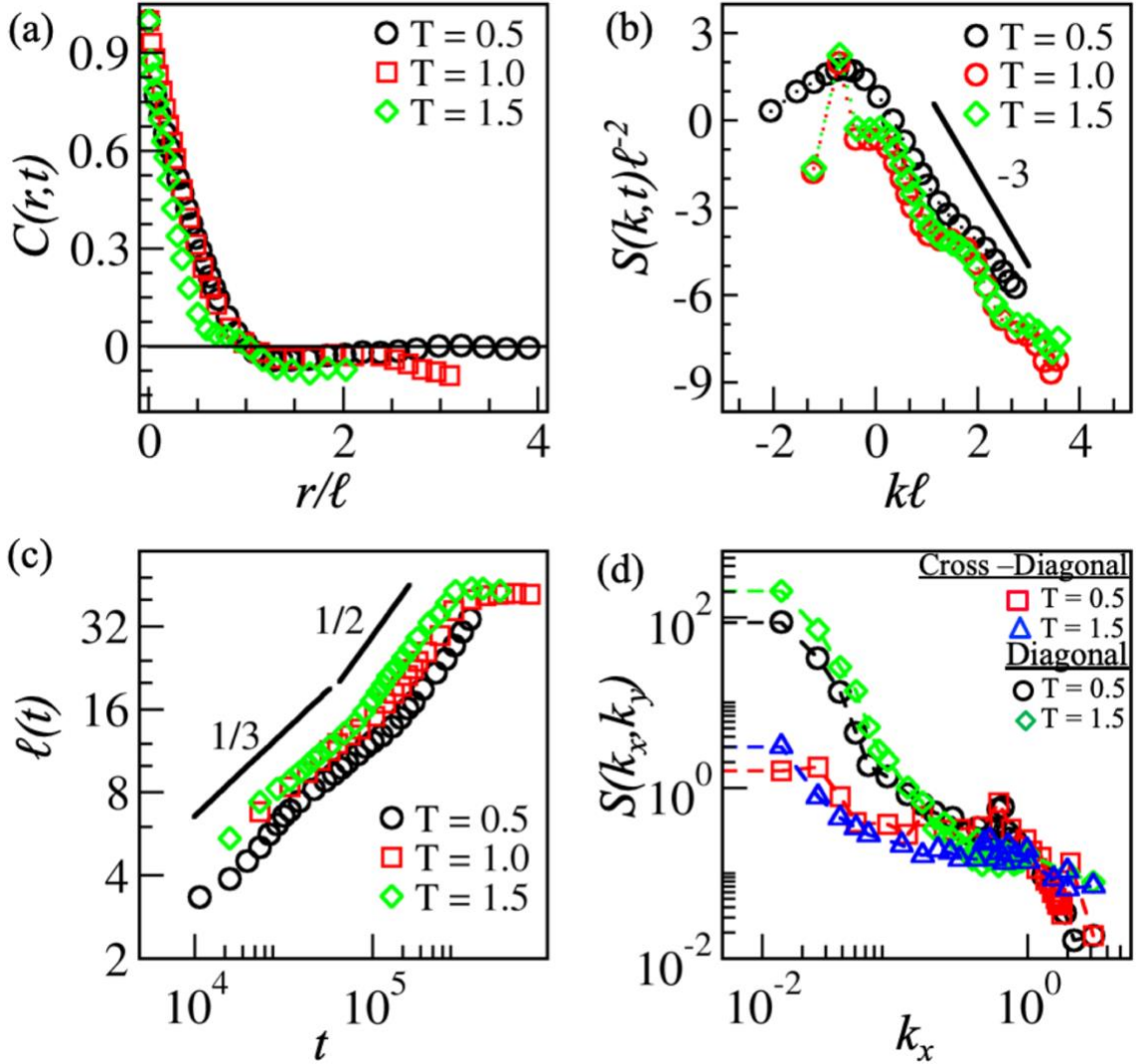


Figure 9: (a) Plot of  $C(r, t)$  vs.  $r/\ell(t)$  (for the evolutions shown in Figs. 7(c), 7(f), and 7(i), respectively) at  $T = 0.5$  (black symbol),  $T = 1.0$  (red symbol), and  $T = 1.5$  (green symbol) for  $t = 4 \times 10^6$  at  $N_1 = 10\%$ . (b) Plot of  $S(k, t)\ell(t)^{-2}$  vs.  $k\ell(t)$  corresponding to the data sets in (a). (c) Log-log plot of length scale,  $\ell(t)$  vs.  $t$ . (d) The comparison of  $S(k_x, k_y)$  along the lattice diagonals for morphologies at  $T = 0.5$  and  $T = 1.5$ .

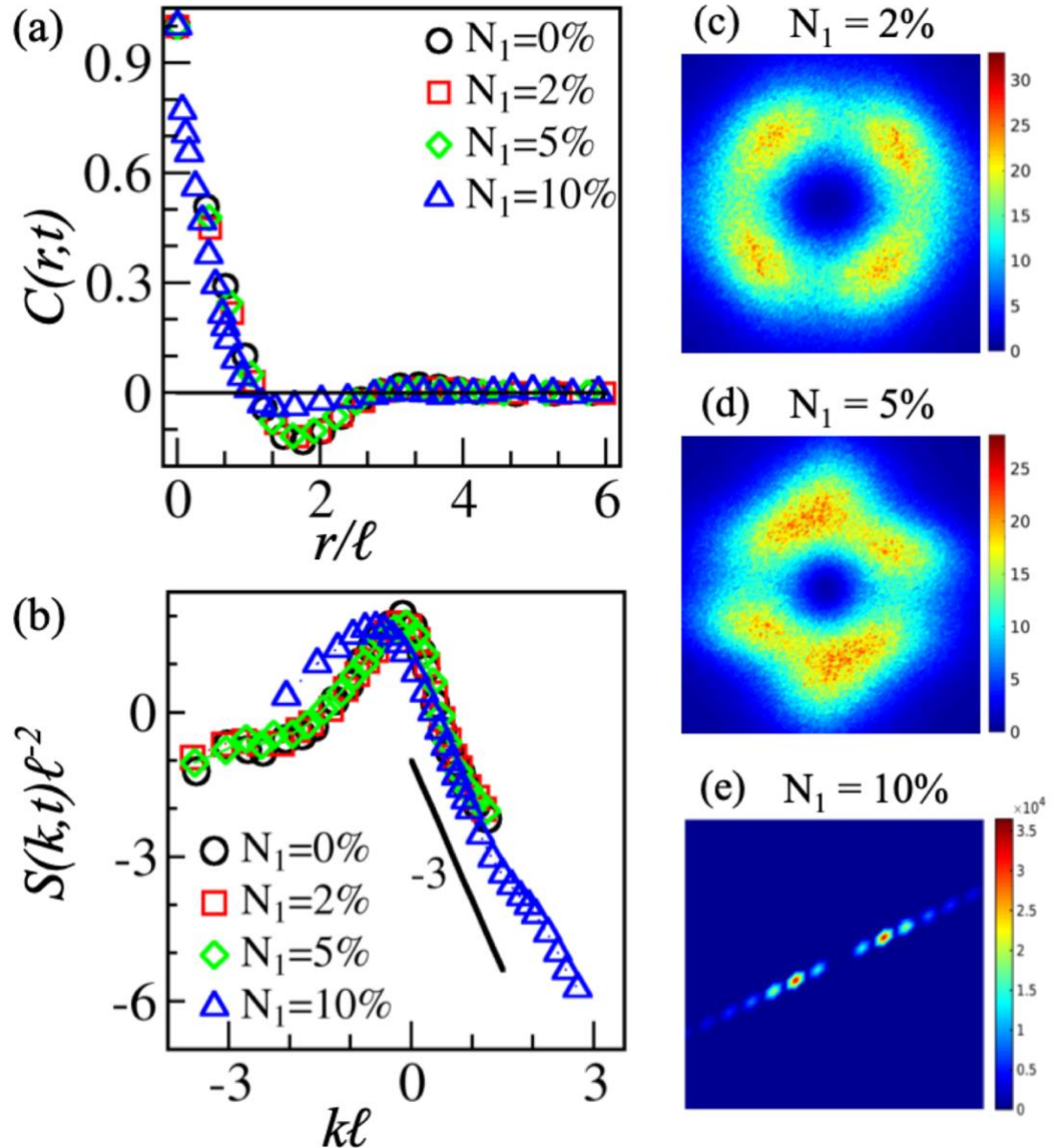


Figure 10: (a) Plot of  $C(r, t)$  vs.  $r/\ell(t)$  for various percentages of disordered,  $N_1 = 0\%$ ,  $2\%$ ,  $5\%$ , and  $10\%$  at  $T = 0.5$ . (b) Plot of  $S(k, t)\ell(t)^{-2}$  vs.  $k\ell(t)$  for the data sets in (a). The spatial variation of scattering intensity at  $t = 4 \times 10^6$  MCS and  $T = 0.5$  for  $N_1 = 2\%$  in (c),  $N_1 = 5\%$  in (d), and  $N_1 = 10\%$  in (e).